## RESEARCH ARTICLE

# Pressure-induced reversible framework rearrangement and increased polarization in the polar [NH4][Cd(HCOO)3] hybrid perovskite†

Juan Manuel Bermúdez-García, [ID] [a] Alberto García-Fernández, [ID] [a] Adrián Andrada-Chacón, [ID] [b] Javier Sánchez-Benítez, [ID] [b] Wei Ren, [ID] [c,d] Shunbo Hu, [ID] [c,d] Teng Gu, [e] Hongjun Xiang, [ID] [e] Malgorzata Biczysko, [ID] [f] Socorro Castro-García, [ID] [a] Manuel Sánchez-Andújar, [ID] *[a] Alessandro Stroppa [ID] *[g] and María Antonia Señarís-Rodríguez [ID] [a]

In this work, we study the structural changes of the polar [NH4][Cd(HCOO)3] hybrid perovskite under external hydrostatic pressure. We report a reversible framework rearrangement as a function of pressure characterized by: (i) a gradual modification of one formate ligand, which changes its coordination mode from a bridging *syn–anti* mode at atmospheric pressure (LP-phase) to a *chelating-anti* mode at high-pressure (HP-phase) and (ii) a change in the coordination of the $Cd^{2+}$ cations from six-coordinated (LP-phase) to hepta-coordinated (HP-phase). Very interestingly, this unprecedented framework arrangement displays a large electrical polarization. For instance, the polarization value observed at $p$ = 17.7 GPa is about four times the polarization at atmospheric pressure. Therefore, we report that the external pressure induces a novel framework rearrangement in the polar [NH4][Cd(HCOO)3] hybrid perovskite with enhanced electrical polarization. This structure–property relationship offers new insights for designing novel ferroelectric materials based on pressure-responsive hybrid perovskite materials.

## Introduction

Hybrid organic–inorganic perovskites (HOIPs) are an emerging class of materials with (multi)functional properties of interest for technological applications. They have been found to display a large variety of physical properties[1,2] (*i.e.* magnetism,

*[a]Department of Chemistry, Faculty of Sciences and CICA, University of A Coruña, Campus A Coruña, 15071 A Coruña, Spain. E-mail: msanchez@udc.es*

*[b]MALTA-Consolider Team, Departamento de Química Física, Facultad de Ciencias Químicas, Universidad Complutense de Madrid, 28040 Madrid, Spain*

*[c]Department of Physics and International Center of Quantum and Molecular Structures, Shanghai University, Shanghai 200444, China*

*[d]Materials Genome Institute, Shanghai Key Laboratory of High Temperature Superconductors, Shanghai University, Shanghai 200444, China*

*[e]Key Laboratory of Computational Physical Sciences (Ministry of Education), State Key Laboratory of Surface Physics, Department of Physics, Fudan University, Shanghai 200433, China*

*[f]International Centre for Quantum and Molecular Structures (ICQMS), College of Sciences, Shanghai University, 99 Shangda Road, 200444 Shanghai, China*

*[g]CNR-SPIN, c/o Dip.to di Scienze Fisiche e Chimiche, Via Vetoio, 67010 Coppito, AQ, Italy. E-mail: alessandro.stroppa@spin.cnr.it*

†Electronic supplementary information (ESI) available: Detail of PXRD patterns and Le Bail refinement of [NH4][Cd(HCOO)3] upon compression at room temperature. Diagram showing the main changes on the crystal structure caused by applied external pressure. See DOI: 10.1039/c9qi00749k

ferroelectricity, multiferroicity, photoconductivity), which were traditionally associated with transition metal oxides with a perovskite structure (pure inorganic perovskites).[3,4]

Similar to pure inorganic perovskites, HOIPs also display a general formula ABX₃. Nevertheless, in this case the A-site and/or the X-site are occupied by organic cations and/or organic ligands, respectively. Specially well-known are the families with A = organic cations and X = halides (hybrid halide perovskites)[5] or those with A = $NH_4^+$ or organic cations and X = organic anions, such as the hybrid formate perovskites with X = $HCOO^-$.[2]

An important consequence of the incorporation of molecular components into these compounds is the emergence of new structural degrees of freedom for which there is no analogue in conventional perovskites, such as the so-called "forbidden" tilts and the columnar shift degree of freedom.[6] More importantly, their large structural and chemical diversity offers substantial opportunities for tuning their physical properties by suitable chemical modification.[7,8] In addition, HOIPs can also respond to different types of physical and chemical stimuli, such as light,[1] pressure,[9] temperature,[10] and electric[11,12] and magnetic fields.[13]

Since HOIPs are rather soft and flexible materials, the application of external hydrostatic pressure can induce different dis-

This journal is © the Partner Organisations 2019

*Inorg. Chem. Front.*, 2019, **6**, 2379–2386 | 2379

tortions within the framework. Therefore, these materials can display different types of transformations,[14–16] such as amorphization,[17,18] and metallization,[19] as well as non-reversible[20,21] and reversible phase transitions.[22–24] Very interestingly, the external pressure can enhance functional properties, such as in the case of photovoltaic perovskites,[25,26] which have been recently rather intensively studied in this regard. Moreover, pressure can induce completely new properties, such as the barocaloric effects[27] recently reported for the [TPrA][M(dca)$_3$] perovskites (TPrA = tetrapropylammonium cations, M = Mn$^{2+}$ and Cd$^{2+}$, dca = dicyanamide ligands).[28,29]

Nevertheless, and at difference with halide perovskites, fundamental high-pressure studies on hybrid perovskites remain relatively much more scarce, probably due to their intrinsic structural complexity. And as is well known, such studies would be very useful for gaining insights into the origin of pressure–structure–property relationships. Eventually, they could even lead to the discovery of new polymorphs or shed light on new materials with improved properties.[30]

With this aim, in this work we have focused on the hybrid organic–inorganic compound with X = formate [NH$_4$][Cd(HCOO)$_3$] with a perovskite-like structure. As we had previously reported,[31] this compound is polar and external pressure markedly increases its polarization (observed by second harmonic generation SHG studies) and induces several phase transitions around 2.5, 6, 10 and 14 GPa (as observed by Raman spectroscopy),[31] whose nature and characteristics remain to be clarified. At room temperature and ambient pressure, this compound displays a [Cd(HCOO)$_3$]$^-$ framework showing a $4^{12}\cdot6^3$ topology and a perovskite-like architecture with a combination of different structural distortions, which are responsible for the polar nature of this compound.[31,32] Moreover, this compound is singular and unique (among all the up-to-date reported hybrid metal formates with a perovskite structure) because the Cd$^{2+}$ cations are connected by bridging HCOO$^-$ anions, where all display only a *syn–anti* coordination mode.[31] In that context, it should be remembered that even if the bidentate bridge is the usual coordination mode between two metal cations in HOIPs,[33] the *anti–anti* coordination mode is by far the predominant one, even if there are a couple of examples of coexistence of *syn–anti* and *anti–anti* formate bridges in other compounds.[31]

In addition, as recently reported, the coordination of the formate ligand can be switched by an external stimulus (*i.e.* temperature and pressure), thus inducing relevant changes in the crystal structure of the given compound.[34,35]

Taking into account this background, in this work we try to shed light on the structural changes and polarization enhancement driven by the application of hydrostatic pressure in the polar [NH$_4$][Cd(HCOO)$_3$] compound, previously suggested by SHG and Raman studies.

To achieve this aim, we have made combined efforts to address this challenge with two new approaches, namely by high-pressure powder X-ray diffraction (PXRD) experiments carried out using a conventional X-ray radiation source together with density functional theory (DFT) calculations.

# Experimental

***Caution!*** Compounds containing cadmium are highly toxic. Care must be taken when handling the samples, and appropriate disposal procedures are required.

## Synthesis

Cd(ClO$_4$)$_2$·$x$H$_2$O (Aldrich), HCOONH$_4$ (99.995%, Panreac), absolute methanol (99.5% Panreac) and formic acid (98%, Fluka) were commercially available and used as purchased without further purification.

For the synthesis, 4 mL of a methanol solution containing 0.1 M Cd(ClO$_4$)$_2$·$x$H$_2$O were placed at the bottom of a glass tube. Upon the Cd$^{2+}$ solution, 4 mL of a methanol solution containing 0.8 M HCOONH$_4$ and 0.4 M HCOOH were carefully layered. The tube was sealed and kept undisturbed, and colourless crystals with plate morphology were obtained after 2 weeks. They were washed with ethanol and dried at room temperature.

## High-pressure powder X-ray diffraction (PXRD) studies

High-pressure powder X-ray diffraction measurements have been carried out with a modified Merrill–Bassett Diamond Anvil Cell (DAC), coupled to an Xcalibur diffractometer. PXRD patterns were collected on a 135 mm Atlas CCD detector, placed at 90 mm from the sample using a Kα1 : Kα2 molybdenum anode. The X-ray beam was collimated to a diameter of 300 μm. A stainless-steel gasket pre-indented to a thickness of 80 μm was used. A 250 μm diameter hole was drilled in the gasket, in which the sample was located. The diamond anvils used have 600 μm culets. Finally, silicone oil was used as a pressure-transmitting medium and several ruby chips were distributed in the pressure chamber for measuring the pressure by the ruby fluorescence method. CRYSALIS software was used for data collection and preliminary data reduction.

The obtained PXRD patterns were analyzed by Le Bail profile analysis using the GSAS[36] and EXPGUI[37] software.

## Density functional theory (DFT) calculations

The density functional theory (DFT) method has been used for studying the structural properties and for estimating the electric polarization. The ion-electron interaction is described by the projector augmented wave (PAW) method[38,39] as implemented in the Vienna *ab initio* simulation package (VASP).[40,41] For the exchange–correlation potential we used the PBE[42] approximation. The plane-wave cut-off energy is set to 550 eV, and all the atoms are allowed to relax until atomic forces are smaller than 0.01 eV Å$^{-1}$ on any ion. The electric polarization is computed by the Berry phase method[35,43–45] by building an appropriate antiferroelectric (AFE) reference state and considering a suitable path in the configurational space connecting to the ferroelectric (FE) state.[46] In order to save computational time and to simplify the path, after atomic optimization the NH$_4^+$ atoms were replaced by K$^+$ atoms at the same atomic position of the N atom of the organic cation, while all the other atoms are frozen at previously relaxed atomic positions.

2380 | *Inorg. Chem. Front.*, 2019, **6**, 2379–2386

This journal is © the Partner Organisations 2019

For each structure under different pressures, we studied the pressure-induced phase transitions using the swarm-intelligence CALYPSO method,[47,48] which enables a global minimization of free-energy (reduced to enthalpy at 0 K) surface merging first-principles total-energy calculations. The method is specially designed for the global search of ground-state structures at a given chemical composition and under external conditions (*i.e.* pressure) unbiased by any known structural information, and it has been successfully applied to predictions of high-pressure phases of various systems.[49–53]

The Raman spectra have been simulated at the DFT level for the cluster unit $[Cd(HCOO)_6]^{4-}$, mimicking either ambient pressure or high pressure atoms arrangements. The computations have been performed with the B3LYP[54] functional including D3(BJ)[55,56] dispersion correction, which allows good reproduction of vibrational spectra in the solid state by cluster models.[57] The basis set 6-31+G(d,p) has been used for H, C and O atoms in conjunction with the Stuttgart-Dresden electron core pseudopotential[58] for the Cd.[59] These computations employed the Gaussian suite of programs.[60]

## Results and discussion

### High-pressure PXRD experiments

We have studied the crystal structure evolution of the $[NH_4][Cd(HCOO)_3]$ perovskite under pressure by *in situ* high-pressure PXRD experiments. The obtained patterns of $[NH_4][Cd(HCOO)_3]$ from atmospheric pressure ($p_{atm}$) to 17.7 GPa are shown in Fig. 1.

A smooth evolution of the PXRD patterns with applied pressure is observed, without any dramatic change in response to external pressure, not even at the pressures for which Raman spectroscopy under pressure suggested the existence of phase transitions.[31] Nevertheless, a more careful look at the obtained patterns (whose limited resolution is due to the complexity of the DAC experimental setup) reveals several pressure-driven phase transitions. These transitions are evidenced by the splitting of some peaks, the broadening of other peaks, and the appearance of new diffraction peaks under the applied pressure. It should be noted that such pressure-driven structural modifications are reversible, and the atmospheric pressure crystal structure is recovered after decompression (see Fig. S1 of the ESI†).

In order to study the evolution of the crystal structure with applied pressure, we carried out Le Bail refinement of the obtained high-pressure PXRD patterns (see Fig. S2–S24 of the ESI†).

In this context, and from the evolution of the PXRD patterns as a function of pressure, we concluded that the clearest phase transition occurs around 9.0 GPa, pressure at which Raman spectroscopy also detects a sharp change. Therefore, we focus our studies on such phase transition, even if other weaker changes are also observed at 2.2, 6.3 and 14.3 GPa (also in agreement with our previous Raman spectroscopy results[31]).

According to the Le Bail fitting of the PXRD patterns at around 9.0 GPa, the low-pressure phase (LP-phase) with orthorhombic symmetry (space group $Pna2_1$) transforms into a high-pressure phase (HP-phase) with monoclinic symmetry (space group $Pc$). It should also be noted that in the proposed HP-phase, the *a*- and *c*-axes are swapped with respect to those of the LP-phase (see Fig. 2 and 3).

The evolution of lattice parameters of these two crystal structures under pressure is shown in Fig. 2 and Table S1 of the ESI.† As it can be seen, a sharp decrease of cell parameters and cell volume takes place upon application of pressure around $p \sim 9.0$ GPa (the volume of the HP-phase is around 5.5% smaller than that of the LP-phase), which indicates a first order phase transition with substantial changes in the atomic arrangement. In addition, the HP-crystal structure shows an anisotropic compressibility for pressures above 9.0 GPa, where the cell parameter *c* increases with pressure while the *a* and *b* parameters decrease. As a result, the cell volume remains finally almost constant for *p* > 9.0 GPa. It is worth noting that this unusual phenomenon has also been reported –among framework materials– in $[C(NH_2)_3][Cd(HCOO)_3]$, $InD(bdc)_2$ (bdc = 1,4-benzenedicarboxylate) and $Ag_3[Co(CN)_6]$.[61–63]

The volume–pressure (V–P) data for the LP-phase were fitted (see Fig. S25 of the ESI†) with second-order Birch–Murnaghan (BM) equations of state (EoS) and the isothermal bulk modulus for LP-phase was found to be 32(1) GPa, which lies in the range of values for dense MOFs (~30–58 GPa).[64–66] This value is very similar to the values reported for $[tmenH_2][Er(HCOO)_4]_2$ (tmenH$_2^{2+}$ = *N,N,N′,N′*-tetramethylethylenediammonium), which are about 13.8(4) GPa and 31.5(6) GPa for phases I and II, respectively.[35] The isothermal axial compressibility ($\beta$) of the LP-phase was estimated as $\beta_a = 7.2(2) \times 10^{-3}$ GPa$^{-1}$, $\beta_b = 4.5(2) \times 10^{-3}$ GPa$^{-1}$ and $\beta_c = 6.1(2) \times 10^{-3}$



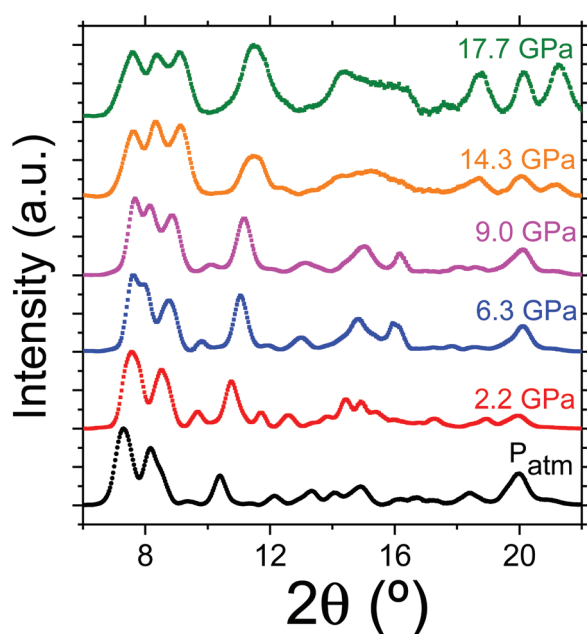**Fig. 1** Representative examples showing the evolution of the PXRD patterns of $[NH_4][Cd(HCOO)_3]$ with pressure, from $P_{atm}$ up to 17.7 GPa, at room temperature.

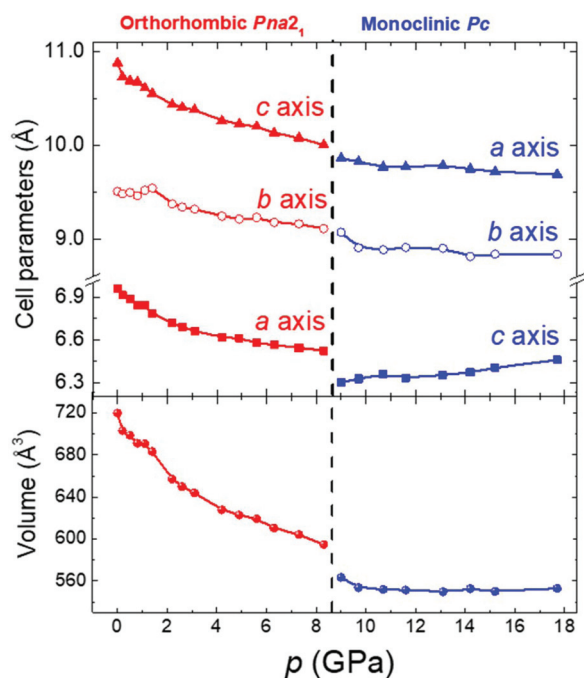**Fig. 2** Unit cell parameters (top) and volume (bottom) of $[NH_4][Cd(HCOO)_3]$ as a function of pressure as obtained from Le Bail fitting of the PXRD-patterns.
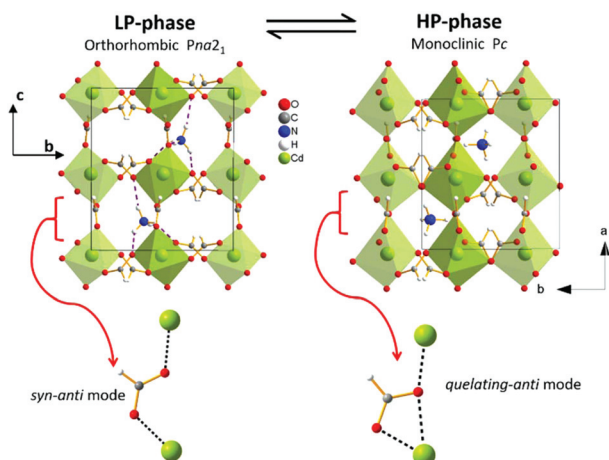


**Fig. 3** (Top) crystal structures of LP- and HP-phases of $[NH_4][Cd(HCOO)_3]$. (Bottom) Details of the coordination mode of the formate ligand, which changes from a *syn–anti* bridging mode in the LP-phase to a chelating-*anti* mode in the HP-phase.

GPa$^{-1}$. The *a* and *c* axes display the greatest degree of compressibility, which confirms that the structure is more easily deformable along these axes.

**Crystal structure at high-pressure from DFT calculations**

In order to elucidate the microscopic mechanism of the structural changes under pressure, the atomic coordinates of the $[NH_4][Cd(HCOO)_3]$ compound at $p_{atm}$, 1.4, 4.2, 8.3, 11.6 and 17.7 GPa were refined by first-principles geometry optimization

(CALYPSO method) based on the experimental cell parameters. The previously reported crystal structure[31] at $p_{atm}$ was employed as the starting structural model.

Once the geometry optimization of the atomic coordinates and cell parameters was reached without the restraint of a space group, taking into account the atomic positions inside the unit cell, we could determine the space group of the obtained crystal structure, which turned out to be *Pc* in the case of the HP-phase. The obtained HP-phase (see Table S2 of the ESI†) can adequately simulate the experimental data obtained from the high-pressure X-ray difraction experiments (see Fig. S26 of the ESI†).

The crystal structure of the HP-phase in comparison with the LP-phase, as well as the structural details of the formate ligand in both phases, is shown in Fig. 3.

According to our results, the HP-phase is described by a polar space group *Pc* and it has an anionic $[Cd(HCOO)_3]^-$ framework with a perovskite-like topology, even if it is very distorted, and where the $NH_4^+$ cations are located inside the resulting and also very distorted cavity.

Surprisingly, in this HP-phase the $Cd^{2+}$ cations are no longer six-coordinated (as in the case of the LP-phase and the "conventional" perovskite structure) but are hepta-coordinated, as shown in Fig. 4. As shown there, in the HP-phase each $Cd^{2+}$ cation is connected to its six nearest neighbour metal cations through six formate bridges, where four of them exhibit a *syn–anti* configuration (within the *bc* plane) whereas another two show a chelating-*anti* mode (along the *a* axis), thus finally resulting in a coordination number of 7 in a "pseudo" pentagonal bipyramid environment. Therefore, the most prominent differences between the LP-phase and HP-phase are: (i) the change of coordination of part of the formate bridges from the *syn–anti* mode in the LP-phase to chelating-*anti* mode in the HP-phase (see Fig. 3), and (ii) the change of coordination of the $Cd^{2+}$ cations from six-coordinated in the LP-phase to hepta-coordinated in the HP-phase (see Fig. 4).

Even if it is well known that the formate ligand can display different coordination modes[67] (*i.e.* mono- and bidentate bridging and chelating modes), and the chelating mode is observed in lanthanide metal-formate systems, this is the first time that such coordination is found in transition metal-
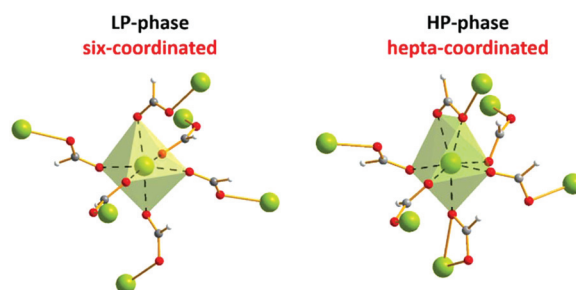


**Fig. 4** Details of the coordination environment of $Cd^{2+}$ cations, namely six-coordinated in the LT-phase (left), and hepta-coordinated in the HP-phase (right).

**2382** | *Inorg. Chem. Front.*, 2019, **6**, 2379–2386

This journal is © the Partner Organisations 2019

formate systems.[68] Moreover, it should be noted that the here observed pressure-induced bond rearrangement is different from those reported in the literature (*i.e.* [EtNH$_3$][Cu (HCOO)$_3$],[34] and [tmenH$_2$][Er(HCOO)$_4$]$_2$[35]) where a change of coordination of the formate ligand from the chelating mode in the LP-phase to *anti–anti* mode in the HP-phase was reported. Even more, examples reporting seven-coordinated Cd$^{2+}$ compounds are very scarce, and none of these compounds are mononuclear or involve monodentate ligands.[69]

From a deeper structural point of view, this complex pressure-driven phase transition is related to the presence of the unusual *syn–anti* bridging coordination mode in the formate ligands of this hybrid organic–inorganic perovskite. In fact it is the rotation of two of these *syn–anti* formate ligands which are along the *c*-axis which gives rise to the modifications observed in this compound upon application of pressure, namely the high deformation of the framework structure, the change of the coordination environment of the Cd$^{2+}$ cations and the change of the coordination mode of part of the formate ligands (see Fig. 4 and sketch in Fig. S27 of the ESI†). In addition, the mentioned rotation of such formate ligands upon compression induces a notable decrease in the Cd$^{2+}$– Cd$^{2+}$ distance along the *c* axis of the LP-phase and along the *a* axis of the HP-phase (see Fig. S27 of the ESI†). The evolution of this distortion can be observed through the variation of the Cd$^{2+}$–O–O angle of the formate ligand and the Cd$^{2+}$–Cd$^{2+}$ distance with applied pressure. As shown in Fig. 5, both parameters exhibit a marked decrease upon compression in the LP-phase and display a sharp change at the phase transition. Additionally, both parameters remain almost constant under compression in the HP-phase.

In order to gain more insight and support for the proposed HP-crystal structure, we have also performed DFT calculations to see if such changes would have a direct and clear reflection in the vibrational spectra of this compound under pressure.

For this purpose, we have carried out DFT calculations to estimate the vibrational frequencies of the ambient pressure phase and the HP-phase at *P* = 17.7 GPa, and obtain a more detailed assignment of the vibration modes. It is worth noting that due to the large amount of atoms at both phases, the

theoretical studies have been performed in a cluster unit [Cd(HCOO)$_6$]$^{4-}$ solution which allows carrying out the calculations without compromising the reliability of obtained results.[23]

Also, taking into account that pressure-induced changes bring about a strong distortion of the anionic framework, and a change in the coordination mode of some of the formate ligands we especially focused on vibrational modes related to HCOO$^-$, such as the O–C–O bending mode [$\nu_3$ (HCOO$^-$)] and the out-of-plane H–C mode [$\nu_6$ (HCOO)$^-$].

According to DFT simulations of the Raman spectrum at ambient pressure, where all formate ligands form *syn–anti* bridges, both [$\nu_3$ (HCOO$^-$)] and [$\nu_6$ (HCOO)$^-$] modes are Raman active and give rise to single peaks at 760 cm$^{-1}$ and 1060 cm$^{-1}$, respectively, in full agreement with the experimental Raman results, see ref. 31 and Fig. S28 of the ESI.†

Very interestingly, DFT Raman simulations show a different situation in the HP phase. In this context DFT results predict that the coexistence of *syn–anti* bridging formate ligands together with chelating-*anti* formate ligands will give rise to the appearance of more signals corresponding to new O–C–O bending modes. And that the vibration related to the bending of the chelating-*anti* bridging ligand will appear at higher wavenumbers than those of the *syn–anti* ones, see Fig. S28 of the ESI.† The reason relies on the stronger constrains of the chelating-*anti* bridging ligand (linked through three Cd–O bonds with two different Cd$^{2+}$ cations), which results in a more hindered O–C–O bending vibration than in the case of the *syn–anti* ligands (linked through two bonds to two different Cd$^{2+}$ cations).

On the other hand, for the out-of-plane H–C mode [$\nu_6$ (HCOO)$^-$] the DFT calculations also predict that it will no longer appear as a signal peak in the Raman spectrum of the HP phase, but split, with new wavenumber vibrations related to the chelating-*anti* bridging ligand and the presence of several inequivalent *syn–anti* ligands. Such softening of the H–C bending mode experienced by the chelating-*anti* ligands in turn implies that the increase in the coordination number of this type of ligand results in a weakening of this internal bond compared to the case of the rest of the *syn–anti* formate ligands.

In addition, the general shortening of the C–H bonds under pressure also results in a slight blue shift of the *syn–anti* bending vibrations compared to the ambient pressure phase.

As shown in Fig. S28 of the ESI,† the experimental high pressure Raman data can be interpreted with the DFT predictions, supporting the here reported HP-phase, where the coexistence of two coordination modes in the formate ligands induces the presence of novel Raman peaks with the expected shifts in their wavenumbers.

### Polarization at high-pressure from DFT calculations

As we already mentioned, both the LT- and HP-phases display a polar structure. Furthermore, the previously reported experimental SHG results suggest a marked increase in polarization upon application of pressure.[31] In this work, to confirm that the proposed high-pressure crystal structure supports an increase of polarization, we have performed DFT calculations.
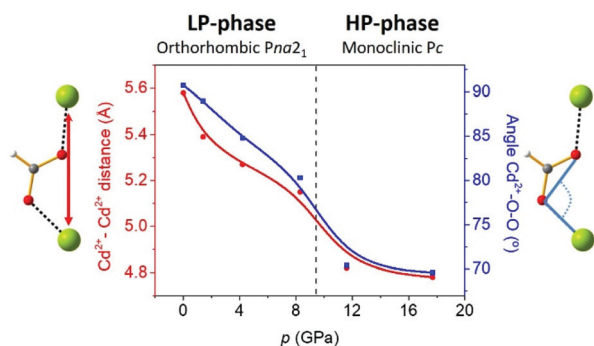


**Fig. 5** Evolution of the Cd$^{2+}$–Cd$^{2+}$ distance and Cd$^{2+}$–O–O angle (showing the rotation of the formate ligand) as a function of pressure.

This journal is © the Partner Organisations 2019

*Inorg. Chem. Front.*, 2019, **6**, 2379–2386 | **2383**

For a given pressure, the optimized structure obtained by CALYPSO has been used to compute the ferroelectric polarization. For a given structure, we introduce a computational reference centric structure which allows us to build an appropriate path for evaluating the polarization. The centric structure has been constructed using a computational crystallographic approach as implemented in the software PSEUDO.[70–72]

As an example, Fig. 6 shows the calculated polarization ($P$) at 17.7 GPa. $\lambda = 0$ represents the centric reference structure, and $\lambda = 1$ represents the optimized ferroelectric structure. A smooth variation of the polarization is obtained along the interpolating path, which ensures that no polarization quanta is included in the calculation.

We have performed the same type of calculation for each different structure corresponding to three different pressures. The calculated polarization as a function of pressure is reported in Fig. 7. From the obtained results it is clear that the pressure-driven polarization is around four times the polarization at $p_{atm}$, with a saturated value of $P \sim 16~\mu C~cm^{-2}$ along the $z$ direction. Our calculations clearly show that the polariz-

ation increases as the pressure increases, in very good agreement with the experimental data.[31]

Therefore, the unprecedented framework arrangement of the HP-phase induces a large polarization in the $[NH_4]$ $[Cd(HCOO)_3]$ perovskite, mainly due to the cooperative tilting of one formate ligand under high pressure. In particular, the cooperative tilting of one formate ligand under external pressure could be related to a large polarization. In order to gain more insights into this phenomena we performed a *functional group analysis* of the polarization.[73] Considering the path connecting the centrosymmetric to the polar structure in the configuration space and starting from the centrosymmetric reference structure, one can activate the atomic displacements corresponding to a particular functional group and evaluate the electric polarization ($P$). For the $ABX_3$ perovskite framework topology, this means that one can calculate $P_A$ and $P_{BX3}$ as the induced polarization due to the atomic displacements at the A site keeping the $BX_3$ framework at the centrosymmetric position, or vice versa. The two contributions usually add linearly to give approximately the total polarization calculated by considering all the correlated atomic displacements (as shown in Fig. 6). In our case, we used such an approach, but the sum of two contributions significantly differs from the total polarization. This suggests that the structure is significantly distorted under high-pressure, so that the linearity in the functional group analysis of the polarization does not hold anymore. However, we have observed that the high-pressure induces correlated atomic distortions, which, collectively, give rise to an increase of polarization. We can conclude here that high-pressure and high-polarization are "positively correlated".

Last, but not least, a comment is in order. It is very well known that the effects of the external pressure can also be driven by internal chemical pressure within the perovskite crystal structure.[74] For this reason, our work opens the door to future challenges for designing novel FE hybrid perovskites with a singular crystal structure and large polarization (as here reported) induced by internal chemical pressure.
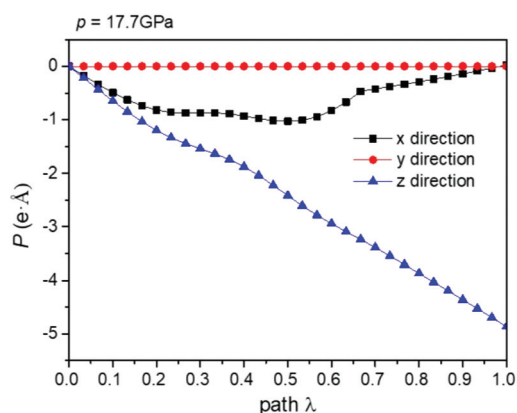


Fig. 6  Calculated polarization for the 17.7 GPa structure along the main directions as a function of path $\lambda$, where $\lambda = 0$ represents the centric structure and $\lambda = 1$ represents the optimized FE structure.

## Conclusions

This work sheds new light on the structural transformations and polarization increase driven by the application of hydrostatic pressure in the polar $[NH_4][Cd(HCOO)_3]$ hybrid perovskite.

This compound displays a reversible framework rearrangement as a function of the applied external pressure, which mainly involves: (i) a change in the coordination mode of one formate ligand from a bridging *syn–anti* mode to a chelating-*anti* mode, and (ii) a change in the coordination of the $Cd^{2+}$ cations, from six-coordinated to hepta-coordinated. Very interestingly, this unprecedented framework arrangement induces a large polarization, $P \sim 16~\mu C~cm^{-2}$.

Therefore, the external pressure is responsible for a singular framework arrangement and a large polarization in the $[NH_4][Cd(HCOO)_3]$ hybrid perovskite.
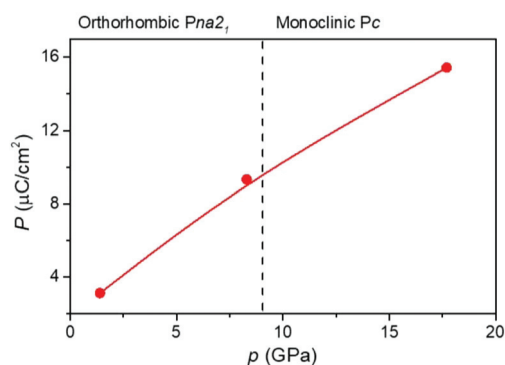


Fig. 7  Calculated polarization ($P$) for different crystal structures as a function of pressure ($p$) along the $z$ direction.

This novel crystal structure highlights the interest in designing novel ferroelectric materials based on pressure-responsive formate ligands. Moreover, this work encourages future studies on similar structural rearrangement and polarization enhancement induced not only by hydrostatic pressure, but also by internal chemical pressure.

## Conflicts of interest

There are no conflicts to declare. All authors have contributed equally to this work.

## Acknowledgements

## Notes and references

1 A. Kojima, K. Teshima, Y. Shirai and T. Miyasaka, *J. Am. Chem. Soc.*, 2009, **131**, 6050–6051.

2 W. Li, Z. Wang, F. Deschler, S. Gao, R. H. Friend and A. K. Cheetham, *Nat. Rev. Mater.*, 2017, **2**, 16099.

3 C. N. R. Rao and B. Raveau, *in Colossal Magnetoresistance, Charge Ordering and Related Properties of Manganese Oxides*, World Scientific, 1998.

4 C. N. R. Rao and J. Gopalakrishnan, *New Directions in Solid State Chemistry*, Cambridge University Press, Cambridge, 2nd edn, 1997.

5 B. Saparov and D. B. Mitzi, *Chem. Rev.*, 2016, **116**, 4558–4596.

6 H. L. B. Boström, J. A. Hill and A. L. Goodwin, *Phys. Chem. Chem. Phys.*, 2016, **18**, 31881–31894.

7 A. K. Cheetham and C. N. R. Rao, *Science*, 2007, **318**, 58–59.

8 A. K. Cheetham, T. D. Bennett, F.-X. Coudert and A. L. Goodwin, *Dalton Trans.*, 2016, **45**, 4113–4126.

9 J. M. Bermúdez-García, M. Sánchez-Andújar, S. Yáñez-Vilar, S. Castro-García, R. Artiaga, J. López-Beceiro, L. Botana, A. Alegría and M. A. Señarís-Rodríguez, *J. Mater. Chem. C*, 2016, **4**, 4889–4898.

10 J. M. Bermúdez-García, M. Sánchez-Andújar, S. Yáñez-Vilar, S. Castro-García, R. Artiaga, J. López-Beceiro, L. Botana, Á. Alegría and M. A. Señarís-Rodríguez, *Inorg. Chem.*, 2015, **54**, 11680–11687.

11 Y.-M. You, W.-Q. Liao, D. Zhao, H.-Y. Ye, Y. Zhang, Q. Zhou, X. Niu, J. Wang, P.-F. Li, D.-W. Fu, Z. Wang, S. Gao, K. Yang, J.-M. Liu, J. Li, Y. Yan and R.-G. Xiong, *Science*, 2017, **357**, 306–309.

12 W. Zhang and R. Xiong, *Chem. Rev.*, 2012, **112**, 1163–1195.

13 Z. Wang, K. Hu, S. Gao and H. Kobayashi, *Adv. Mater.*, 2010, **22**, 1526–1533.

14 A. Clearfield, *Dalton Trans.*, 2016, **45**, 4100–4112.

15 J. C. Tan and A. K. Cheetham, *Chem. Soc. Rev.*, 2011, **40**, 1059–1080.

16 F.-X. Coudert, *Chem. Mater.*, 2015, **27**, 1905–1916.

17 F. Capitani, C. Marini, S. Caramazza, P. Dore, A. Pisanu, L. Malavasi, L. Nataf, F. Baudelet, J.-B. Brubach, P. Roy and P. Postorino, *J. Phys. Chem. C*, 2017, **121**, 28125–28131.

18 M. Szafrański and A. Katrusiak, *J. Phys. Chem. Lett.*, 2017, **8**, 2496–2506.

19 A. Jaffe, Y. Lin, W. L. Mao and H. I. Karunadasa, *J. Am. Chem. Soc.*, 2017, **139**, 4330–4333.

20 L. Xin, Z. Fan, G. Li, M. Zhang, Y. Han, J. Wang, K. P. Ong, L. Qin, Y. Zheng and X. Lou, *New J. Chem.*, 2017, **41**, 151–159.

21 S. Jiang, Y. Luan, J. I. Jang, T. Baikie, X. Huang, F. O. Saouma, Z. Wang, T. J. White, J. Fang, S. Jiang, Y. Luan, J. I. Jang, T. Baikie, X. Huang, R. Li and O. Felix, *J. Am. Chem. Soc.*, 2018, **140**, 13952–13957.

22 M. Mączka, T. A. da Silva, W. Paraguassu, M. Ptak and K. Hermanowicz, *Inorg. Chem.*, 2014, **53**, 12650–12657.

23 M. Mączka, P. Kadłubański, P. T. C. Freire, B. Macalik, W. Paraguassu, K. Hermanowicz and J. Hanuza, *Inorg. Chem.*, 2014, **53**, 9615–9624.

24 M. Mączka, A. Gągor, N. L. M. Costa, W. Paraguassu, A. Sieradzki and A. Pikul, *J. Mater. Chem. C*, 2016, **4**, 3185–3194.

25 Z. Ma, Z. Liu, S. Lu, L. Wang, X. Feng, D. Yang, K. Wang, G. Xiao, L. Zhang, S. A. T. Redfern and B. Zou, *Nat. Commun.*, 2018, **9**, 4506.

26 G. Xiao, Y. Cao, G. Qi, L. Wang, C. Liu, Z. Ma, X. Yang, Y. Sui, W. Zheng and B. Zou, *J. Am. Chem. Soc.*, 2017, **139**, 10087–10094.

27 J. M. Bermúdez-García, M. Sánchez-Andújar and M. A. Señarís-Rodríguez, *J. Phys. Chem. Lett.*, 2017, **8**, 4419–4423.

28 J. M. Bermúdez-García, M. Sánchez-Andújar, S. Castro-García, J. López-Beceiro, R. Artiaga and M. A. Señarís-Rodríguez, *Nat. Commun.*, 2017, **8**, 15715.

29 J. M. Bermúdez-García, S. Yáñez-Vilar, A. García-Fernández, M. Sánchez-Andújar, S. Castro-García, J. López-Beceiro, R. Artiaga, M. Dilshad, X. Moya and M. A. Señarís-Rodríguez, *J. Mater. Chem. C*, 2018, **6**, 9867–9874.

30 A. Katrusiak and P. F. McMillan, *High-Pressure Crystallography*, Springer Netherlands, Dordrecht, 2004.

31 L. C. Gómez-Aguirre, B. Pato-Doldán, A. Stroppa, S. Yáñez-Vilar, L. Bayarjargal, B. Winkler, S. Castro-García, J. Mira,

This journal is © the Partner Organisations 2019

*Inorg. Chem. Front.*, 2019, **6**, 2379–2386 | **2385**

M. Sánchez-Andújar and M. A. Señarís-Rodríguez, *Inorg. Chem.*, 2015, **54**, 2109–2116.

32 H. L. B. Boström, M. S. Senn and A. L. Goodwin, *Nat. Commun.*, 2018, **9**, 2380.

33 S. M. Bovill and P. J. Saines, *CrystEngComm*, 2015, **17**, 8319–8326.

34 R. Shang, S. Chen, B. W. Wang, Z. M. Wang and S. Gao, *Angew. Chem., Int. Ed.*, 2015, 2097–2100.

35 E. C. Spencer, M. S. R. N. Kiran, W. Li, U. Ramamurty, N. L. Ross and A. K. Cheetham, *Angew. Chem., Int. Ed.*, 2014, **53**, 5583–5586.

36 A. C. Larson and R. B. Von Dreele, *Los Alamos Natl. Lab. Rep. LAUR 86-748*, 2000.

37 B. H. Toby, *J. Appl. Crystallogr.*, 2001, **34**, 210–213.

38 P. E. Blöchl, *Phys. Rev. B: Condens. Matter Mater. Phys.*, 1994, **50**, 17953–17979.

39 G. Kresse and D. Joubert, *Phys. Rev. B: Condens. Matter Mater. Phys.*, 1999, **59**, 1758–1775.

40 G. Kresse and J. Furthmüller, *Phys. Rev. B: Condens. Matter Mater. Phys.*, 1996, **54**, 11169–11186.

41 G. Kresse and J. Furthmüller, *Comput. Mater. Sci.*, 1996, **6**, 15–50.

42 J. P. Perdew, K. Burke and M. Ernzerhof, *Phys. Rev. Lett.*, 1996, **77**, 3865–3868.

43 R. D. King-Smith and D. Vanderbilt, *Phys. Rev. B: Condens. Matter Mater. Phys.*, 1993, **47**, 1651–1654.

44 D. Vanderbilt and R. D. King-Smith, *Phys. Rev. B: Condens. Matter Mater. Phys.*, 1993, **48**, 4442–4455.

45 R. Resta, *Rev. Mod. Phys.*, 1994, **66**, 899–915.

46 S. Hu, H. Gao, Y. Qi, Y. Tao, Y. Li, J. R. Reimers, M. Bokdam, C. Franchini, D. Di Sante, A. Stroppa and W. Ren, *J. Phys. Chem. C*, 2017, **121**, 23045–23054.

47 Y. Wang, J. Lv, L. Zhu and Y. Ma, *Phys. Rev. B: Condens. Matter Mater. Phys.*, 2010, **82**, 094116.

48 Y. Wang, J. Lv, L. Zhu and Y. Ma, *Comput. Phys. Commun.*, 2012, **183**, 2063–2070.

49 J. Lv, Y. Wang, L. Zhu and Y. Ma, *Phys. Rev. Lett.*, 2011, **106**, 015503.

50 L. Zhu, H. Wang, Y. Wang, J. Lv, Y. Ma, Q. Cui, Y. Ma and G. Zou, *Phys. Rev. Lett.*, 2011, **106**, 145501.

51 Y. Yan, S. Zhang, Y. Wang, G. Yang and Y. Ma, *RSC Adv.*, 2015, **5**, 104426–104432.

52 Q. Li, J. Wang, M. Zhang, Q. Li and Y. Ma, *RSC Adv.*, 2015, **5**, 35882–35887.

53 L. Zhu, H. Liu, C. J. Pickard, G. Zou and Y. Ma, *Nat. Chem.*, 2014, **6**, 644–648.

54 A. D. Becke, *J. Chem. Phys.*, 1993, **98**, 5648–5652.

55 S. Grimme, J. Antony, S. Ehrlich and H. Krieg, *J. Chem. Phys.*, 2010, **132**, 154104.

56 S. Grimme, S. Ehrlich and L. Goerigk, *J. Comput. Chem.*, 2011, **32**, 1456–1465.

57 J. Bloino, M. Biczysko and V. Barone, *J. Phys. Chem. A*, 2015, **119**, 11862–11874.

58 G. Igel-Mann, H. Stoll and H. Preuss, *Mol. Phys.*, 1988, **65**, 1321–1328.

59 A. Bergner, M. Dolg, W. Küchle, H. Stoll and H. Preuß, *Mol. Phys.*, 1993, **80**, 1431–1441.

60 M. J. Frisch, G. W. Trucks, H. B. Schlegel, G. E. Scuseria, M. A. Robb, J. R. Cheeseman, G. Scalmani, V. Barone, G. A. Petersson, H. Nakatsuji, X. Li, M. Caricato, A. V. Marenich, J. Bloino, B. G. Janesko, R. Gomperts, B. Mennucci, H. P. Hratchian, J. V. Ortiz, A. F. Izmaylov, J. L. Sonnenberg, D. Williams-Young, F. Ding, F. Lipparini, F. Egidi, J. Goings, B. Peng, A. Petrone, T. Henderson, D. Ranasinghe, V. G. Zakrzewski, J. Gao, N. Rega, G. Zheng, W. Liang, M. Hada, M. Ehara, K. Toyota, R. Fukuda, J. Hasegawa, M. Ishida, T. Nakajima, Y. Honda, O. Kitao, H. Nakai, T. Vreven, K. Throssell, J. A. Montgomery, Jr., J. E. Peralta, F. Ogliaro, M. J. Bearpark, J. J. Heyd, E. N. Brothers, K. N. Kudin, V. N. Staroverov, T. A. Keith, R. Kobayashi, J. Normand, K. Raghavachari, A. P. Rendell, J. C. Burant, S. S. Iyengar, J. Tomasi, M. Cossi, J. M. Millam, M. Klene, C. Adamo, R. Cammi, J. W. Ochterski, R. L. Martin, K. Morokuma, O. Farkas, J. B. Foresman and D. J. Fox, *Gaussian 16 (Revision B.01)*, Gaussian, Inc., Wallingford CT, 2016.

61 A. L. Goodwin, D. A. Keen and M. G. Tucker, *Proc. Natl. Acad. Sci. U. S. A.*, 2008, **105**, 18708–18713.

62 I. E. Collings, M. G. Tucker, D. A. Keen and A. L. Goodwin, *CrystEngComm*, 2014, **16**, 3498.

63 Q. Zeng, K. Wang and B. Zou, *ACS Appl. Mater. Interfaces*, 2018, **10**, 23481–23484.

64 G. Feng, X. Jiang, W. Wei, P. Gong, L. Kang, Z. Li, Y. Li, X. Li, X. Wu, Z. Lin, W. Li and P. Lu, *Dalton Trans.*, 2016, **45**, 4303–4308.

65 E. C. Spencer, N. L. Ross and R. J. Angel, *J. Mater. Chem.*, 2012, **22**, 2074–2080.

66 M. Zhou, K. Wang, Z. Men, C. Sun, Z. Li, B. Liu, G. Zou and B. Zou, *CrystEngComm*, 2014, **16**, 4084–4087.

67 R. Shang, S. Chen, Z.-M. Wang and S. Gao, *in Encyclopedia of Inorganic and Bioinorganic Chemistry*, John Wiley & Sons, Ltd, Chichester, UK, 2014, pp. 1–23.

68 B. Liu, H.-B. Zheng, Z.-M. Wang and S. Gao, *CrystEngComm*, 2011, **13**, 5285.

69 R. A. Scott, *Encyclopedia of inorganic and bioinorganic chemistry*, Wiley, 2012.

70 E. Kroumova, M. I. Aroyo, J. M. Perez-Mato, S. Ivantchev, J. M. Igartua and H. Wondratschek, *J. Appl. Crystallogr.*, 2001, **34**, 783–784.

71 C. Capillas, M. I. Aroyo and J. M. Perez-Mato, *Z. Kristallogr.*, 2005, **220**, 691–699.

72 C. Capillas, E. S. Tasci, G. de la Flor, D. Orobengoa, J. M. Perez-Mato and M. I. Aroyo, *Z. Kristallogr. - Cryst. Mater.*, 2011, **226**, 186–196.

73 Y. Tian, A. Stroppa, Y.-S. Chai, P. Barone, M. Perez-Mato, S. Picozzi and Y. Sun, *Phys. Status Solidi RRL*, 2015, **9**, 62–67.

74 H. Y. Hwang, T. T. M. Palstra, S.-W. Cheong and B. Batlogg, *Phys. Rev. B: Condens. Matter Mater. Phys.*, 1995, **52**, 15046–15049.